Tiny surface defect inspection of electronic passive components using discrete cosine transform decomposition and cumulative sum techniques

Hong-Dar Lin *

Department of Industrial Engineering and Management, Chaoyang University of Technology, 168 Jifong E. Road., Wufong Township, Taichung County 41349, Taiwan, ROC

Abstract

Passive components, owing to their low or no power consumption, are widely used in modern electronic devices. Nevertheless, tiny defects that often appear in the surface of passive components impair not only their appearances but also their functions. This paper proposes a global approach for the automated visual inspection of tiny surface defects in SBL (Surface Barrier Layer) chips, whose random surface texture contains no repetitions of basic texture primitives. The proposed method, taking advantage of the DCT decomposition and the cumulative sum techniques, does not requires textural features, the lack of which often limits the application of feature extraction-based methods. We apply the cumulative sum algorithm to the odd–odd matrix that gathers most power spectra in the decomposed DCT frequency domain, and select the large-magnitude frequency values that represent the background texture of the surface. Then, by reconstructing the frequency matrix without the selected frequency values, we eliminate random texture patterns and retain anomalies in the restored image. Experimental results demonstrate the effectiveness of the proposed method in inspecting tiny defects in random textures.
© 2007 Elsevier B.V. All rights reserved.

1. Introduction

1.1. Popularity of passive components

There are two kinds of electronic components: (1) passive ones that contribute no power amplification in the circuit system and require only a signal to start their functions (e.g., resistors, capacitors and inductors) and (2) active ones that are capable of controlling currents and creating a switching action in the circuit (e.g., diodes, transistors and integrated circuits). As passive components require low or no power consumption, their importance and popularity have been increasing these years when

energy conservation issues intensify. Consumers of electronic products are asking for better energy efficiency, in addition to smaller sizes, lighter weight, more stylish outlooks, etc. The number of passive components used in Printed Circuit Boards (PCBs) has grown to a large extent in much smaller electronic products. More than 80% of the parts in a motherboard are composed of passive components [1,2]. Also, the sizes of passive components have shrunk to $5 \times 2.5 \times 2.5$ mm for sophisticated products [3].

1.2. Surface defects of passive components

With the popularity of passive components, inspection of surface defects has become a critical task for manufacturers who strive to improve product quality and production efficiency of passive components. Surface defects

---
* Tel.: +886 4 2332 3000x4258; fax: +886 4 2374 2327.
  E-mail addresses: hdlin@cyut.edu.tw, hdlin001@yahoo.com.tw

affect not only the appearances of passive components but also their functionality, efficiency and stability. Large and obvious surface defects such as indents, scraps and scratches are usually inspected by automated visual inspection systems [3–8]. But tiny surface flaws such as dust, cavities and pinholes are very difficult to detect because of their extremely small sizes. Tiny surface defects, frequently occurring in the manufacturing process of passive components, cause much greater harms and impact when they appear in high-tech products than in industrial parts. Therefore, to survive in today's competitive market of high-tech products, manufacturers of passive components simply can not afford to ignore tiny surface defects.

To contribute to the field of surface defect inspection on passive components, this research uses disk-like Surface Barrier Layer (SBL) chips as testing samples. SBL chips are passive components (ceramics capacitors) commonly used in many electronic appliances. With a thickness of 0.05 mm and a diameter of 7 mm, SBL chips are small in size, light in weight, and suitable for large-lot-sized production. However, in the surfaces of SBL chips often exist tiny defects that cause problems such as unstable and non-conforming capacitance although the defects occupy only an extremely small area. For a SBL chip image of 256×256 pixels, the size of its tiny defect falls within the range of 1–15 pixels and occupies 0.0015–0.0229% of the image area. Surface defects of this magnitude are defined as tiny defects in this research. Fig. 1 shows SBL samples with tiny defects marked in circles.

Currently, the most common detection methods for passive component defects are human visual inspection and electrical functional tests. Human visual inspection is tedious, time-consuming and highly dependent on the inspectors' experiences, conditions, or moods. Erroneous judgments are easily made because of inspectors' subjectiv-ity and eye fatigues. Electronic functional tests are inherently limited to offline operations and are normally conducted after passive components have been fabricated. Difficulties exist in precisely inspecting tiny flaws by machine vision systems because when product images are being captured, the area of a tiny flaw could expand, shrink or even disappear due to uneven illumination of the environment, complex texture of the product surface, and so on. Seeing the great need for a real-time, compute-aided, visual detection scheme for passive component defects, we propose a discrete cosine transform (DCT)-based image reconstruction approach to overcome the difficulties of traditional machine vision systems.

1.3. Defect detection methods

This paper proposes a global approach for the automated visual inspection of tiny surface defects in SBL chips, whose random surface texture contains no repetitions of basic texture primitives. Generally, automated visual inspection techniques for defects fall into two categories. Approaches of the first category detect defects by comparing the testing image with a pre-stored faultless item through a pixel-to-pixel or template-to-template matching process. Disadvantages of the first category include: (1) time consuming of the matching process, (2) sensitivity to noises, and (3) large data storage needed for the pre-stored templates and the matching process [9,10]. Approaches of the second category select and compute a set of textural features in a sub-image, and then compare the feature values with those of the faultless image to find significant differences. Disadvantages of the second category include: (1) difficulties in deciding what valuable features to extract for texture discrimination, (2) failure of the valuable features of a specific texture in depicting other texture patterns, (3) time consuming of the training process
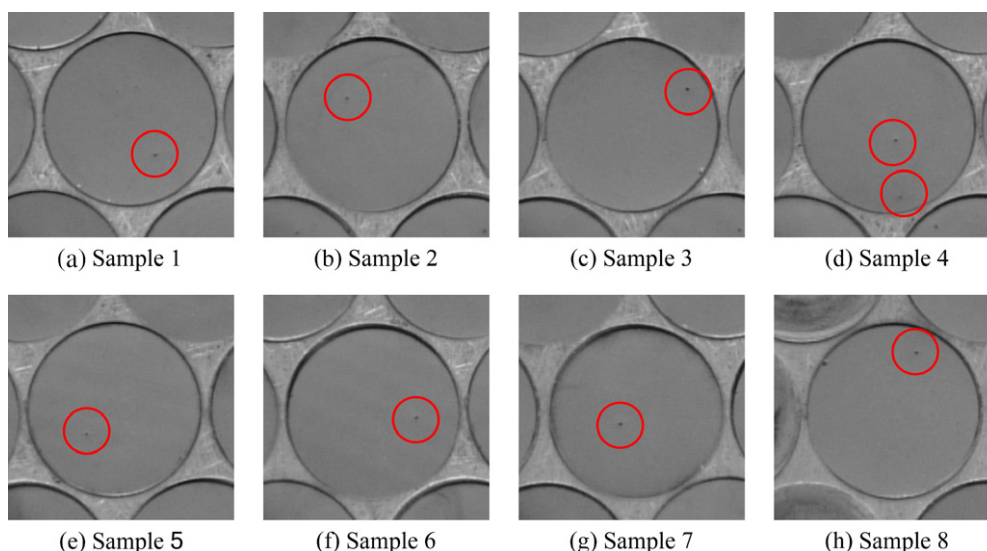

Fig. 1. Samples of SBL chips with tiny surface defects.

(a) Sample 1   (b) Sample 2   (c) Sample 3   (d) Sample 4

(e) Sample 5   (f) Sample 6   (g) Sample 7   (h) Sample 8

for the addition of a new texture, and (4) sophisticated classifiers needed to discriminate texture classes when a vector of multiple features results in high dimensionality [4,11].

Textures can be divided into two types: structural and statistical [12]. Structural textures consist of repetitions of basic texture primitives such as lines, arcs or circles. Commonly found in textile fabrics, structural textures have regular and homogeneous properties. On the other hand, statistical textures do not possess repetitive primitives or regular patterns. They arise randomly in the surfaces of objects such as sandpaper and leather.

Techniques that analyze textures based on local features can also be classified into two kinds: the spatial domain and the frequency domain. First, a traditional technique in the spatial domain is the co-occurrence matrix method. Siew et al. [13] use two-order gray level statistics to build up probability density functions of intensity changes and apply the co-occurrence matrices to evaluate levels of carpet wear. Amet et al. [14] present co-occurrence matrices based on wavelet sub-image characteristics to detect defects of textile fabrics. Second, techniques in the frequency domain extract textural features by conducting frequency transforms such as Fourier transforms, Gabor transforms, or wavelet transforms. Among the frequency transforms, wavelet transforms have been a popular alternative for extracting textural features these years. For example, Tico et al. [15] apply the wavelet transform of the frequency domain to the field of finger-print recognition. Sari-Sarraf and Goddard [16] present a wavelet-based preprocessing module for the detection and localization of woven fabric defects.

Some global approaches have also been developed to detect defects without relying on local features of textures. Tsai and Hsieh [4] present a new approach for the automatic inspection of defects in directionally textured surfaces such as textile fabrics and machined surfaces. Tsai and Huang [5] propose a global approach for the automatic inspection of defects in randomly textured surfaces such as sandpaper, castings, leather, and many other industrial materials. Both of the above two methods make use of the Fourier transform and are based on global image restoration and reconstruction schemes. Tsai and Chiang [11] present a wavelet-based multiresolution approach for the inspection of local defects embedded in homogeneously textured surfaces, such as machined surfaces, natural wood, sandpaper and textile fabrics. By properly selecting wavelet parameters, the wavelet-based multiresolution approach can effectively remove the global repetitive texture pattern and reserve only local anomalies in the restored image.

As to inspecting surface flaws of electronic components, some machine vision systems have been applied to PCBs [9,17], Ball Grid Array (BGA) substrate conducting paths [10], and capacitor chips of passive components [3,18]. Lu and Tsai [6], and Lu and Tsai [7] use singular value decomposition to inspect surface defects of Thin Film Transistor-Liquid Crystal Display (TFT-LCD) panels. Jiang et al. [8] apply analysis of variance and exponentially weighted moving average techniques to uniformity defect inspection of LCD displays.

1.4. DCT-based approaches

The inspection task of this paper involves detecting novel but obscurely faulty items, tiny defects on electronic passive components. Many of these unanticipated defects are extremely small in size and can not be described by explicit measures, thus making automated defect detection difficult. Consequently, we present a new global image reconstruction scheme using DCT for tiny surface defect detection.

Ahmed et al. [19] first define DCT as one-dimensional (1-D) and suitable for 1-D digital signal processing. Most of the researchers that apply DCT for image processing focused on image compression and image reconstruction [20–22], because DCT has the property of packing the most information into the fewest coefficients [23,24]. However, due to the lack of an efficient algorithm, DCT had not been applied as widely as its properties imply. Only until recently, many algorithms and VLSI architectures for the fast computation of DCT have been proposed [25–27].

As most coefficients in the DCT domain are small and can be quantized to zero, manipulating data in the DCT domain is an efficient way to save computer resources [23]. To enhance edges of remote sensing image data in the DCT domain, Chen et al. [28] develop new and fast algorithms that involve three steps: high-pass filtering, gray levels adding, and contrast stretching. Hasan et al. [29] present an improved thresholding technique for speech enhancement in the DCT domain. Kim and Han [30] derive DCT properties related to a standard discontinuity and propose a model-based discontinuity evaluation technique in the DCT domain. This technique is efficient in detecting discontinuities and robust against noise.

Since DCT has the advantages of packing the most information into the fewest coefficients and minimizing reconstruction errors, only a small amount of information of a detailed image will be lost during the image processing procedures [23,24,31]. Such advantages make DCT suitable and favorable for our study of tiny defect detection. The main information, or the approximation, of an image can be represented by a few DCT frequency values of large magnitude. The remaining frequency values of small magnitude provide detailed information of the image. Since the SBL surface has random structures, the larger frequency values retain the information of the statistical patterns and the smaller frequency values retain that of anomalies in the SBL surface. In the application of SBL defect inspection, we can set the larger frequency values to zero and reserve the smaller frequency values to reconstruct the image. Then, the background texture can be removed and

anomalies can be distinctly enhanced in the restored image accordingly.

Requiring neither textural features for detection of local anomalies nor a reference image for comparison, the proposed method avoids the limitations of feature extraction and template matching methods. By regarding an input image as a matrix, we can perform the DCT transformation to transform a spatial domain image into the frequency domain. From the energy concentration analysis of the DCT domain, we can decompose the frequency matrix into four decomposed matrices. We select the proper number of larger frequency values to represent the random structure features of the SBL surface. Then, we set the selected frequency values to zero and reconstruct the image. For a faultless SBL chip, the reconstruction process will result in a uniform image. For a defective SBL chip, the anomalies will be reserved and the random patterns will be eliminated in the restored image. Finally, the entropy method is applied to set the threshold for distinguishing between defective regions and uniform regions in the restored image.

The rest of this paper is organized as follows. Section 2 introduces the properties of DCT and presents the image reconstruction scheme for inspecting tiny surface defects of SBL chips. Also discussed in this section are the selection of the proper sector radius of the DCT frequency components by the cumulative sum algorithm and the defect separation of the restored image by the entropy method. Section 3 presents the results of the experiments on real SBL chips and evaluates the sensitivity of the selected radius and the changes of illumination intensity in lighting conditions. Last but not least, Section 4 concludes with our contributions and suggestions.

2. Proposed defect detection scheme

2.1. The DCT energy analysis of passive component chips

Eq. (1) gives the expression for computing the DCT of a digital image $d_{x,y}$ of size $M \times N$. This expression must be computed for all values of $u = 0, 1, 2, \ldots, M - 1$, and also for all values of $v = 0, 1, 2, \ldots, N - 1$. Similarly, given $D_{u,v}$, we can obtain $d_{x,y}$ via the inverse DCT transform, as shown in Eq. (2) for $x = 0, 1, 2, \ldots, M - 1$ and $y = 0, 1, 2, \ldots, N - 1$. Eqs. (1) and (2) comprise the two-dimensional DCT pair. While u and v are frequency variables, x and y are spatial variables.

$$D_{u,v} = \rho(u)\rho(v) \sum_{x=0}^{M-1} \sum_{y=0}^{N-1} d_{x,y} \cos\left[\frac{(2x+1)u\pi}{2M}\right] \cos\left[\frac{(2y+1)v\pi}{2N}\right] \quad (1)$$

$$d_{x,y} = \sum_{u=0}^{M-1} \sum_{v=0}^{N-1} \rho(u)\rho(v) D_{u,v} \cos\left[\frac{(2x+1)u\pi}{2M}\right] \cos\left[\frac{(2y+1)v\pi}{2N}\right] \quad (2)$$

where

$$\rho(u) = \begin{cases} \sqrt{\frac{1}{M}}, & u = 0 \\ \sqrt{\frac{2}{M}}, & u = 1, 2, 3, \ldots, M - 1 \end{cases},$$

$$\rho(v) = \begin{cases} \sqrt{\frac{1}{N}}, & v = 0 \\ \sqrt{\frac{2}{N}}, & v = 1, 2, 3, \ldots, N - 1 \end{cases},$$

$$\begin{cases} u = 0, 1, 2, \ldots, M - 1 \\ v = 0, 1, 2, \ldots, N - 1 \\ x = 0, 1, 2, \ldots, M - 1 \\ y = 0, 1, 2, \ldots, N - 1 \end{cases}$$

The power spectrum $P(u, v)$ of image $d_{x,y}$ is defined as:

$$P(u, v) = |D_{u,v}|^2 \quad (3)$$

That is, the energy of the image can be obtained by adding up the squares of the DCT coefficients [23].

As the origin of the DCT coefficients has a very huge frequency value, it is sometimes called the Direct Current (DC) component of the spectrum, while other coefficients are called the Alternating Current (AC) components. The DC coefficients in the upper left corner reflect information of lower frequencies, whereas the AC coefficients in the lower right corner reflect that of higher frequencies. DCT has the property of concentrating the dominant energy of a typical image in the low-frequency components. This means that the coefficients of the high-frequency components are close to zero, and therefore negligible in most cases [31].

Fig. 2(a) displays an SBL chip with a faultless surface, and Fig. 2(b) one with a defective surface. Fig. 2(c) and (d) are the DCT domain images of (a) and (b), respectively, while Fig. 2(e) and (f) present their energy plots in 3D perspective. We can see clearly in Fig. 2(e) and (f) that the high-energy frequency components concentrate around the top left origin in the DCT spectrum. Owing to the small size of the tiny defect, the spread sector of the defective surface is not visually different from that of the faultless surface. This indicates that the regular texture pattern is blurred while the anomaly is reserved by restoring only the frequency components that are outside the sector of a properly selected radius.

Let r^* denote the selected radius of the sector in the DCT domain. Let $r^* = 11$ for the faultless surface (Fig. 2(a) and (c)), and $r^* = 15$ for the defective surface (Fig. 2(b) and (d)), which are selected to reconstruct the textured images. Fig. 3(c) and (d) present the reconstruction results after all frequency components outside the selected sector are set to zero. The restored images in Fig. 3 show that the blurred approximated images of the SBL surfaces, and the random patterns and edges are nearly eliminated in the faultless and the defective surfaces.

Fig. 4(c) and (d) present the reconstruction results after all frequency components inside the selected sector are set to zero. The restored images in Fig. 4 show that the tex-
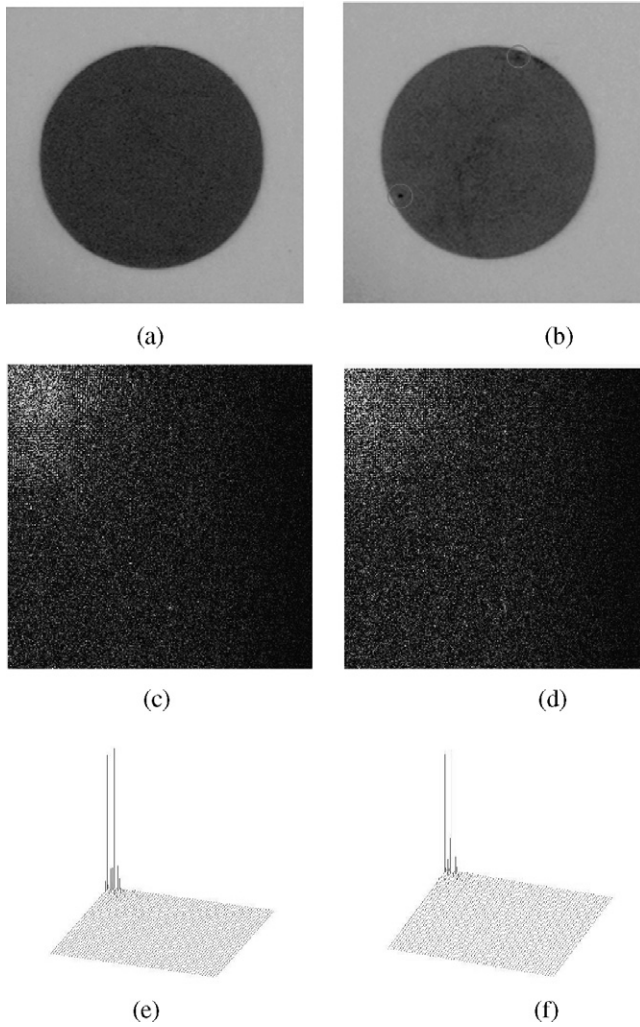
(a)

(b)

(c)

(d)

(e)

(f)

Fig. 2. (a) An SBL chip with a faultless surface; (b) an SBL chip with a defective surface; (c) and (d) the respective DCT domain images; (e) and (f) the respective power spectra in 3D perspective.
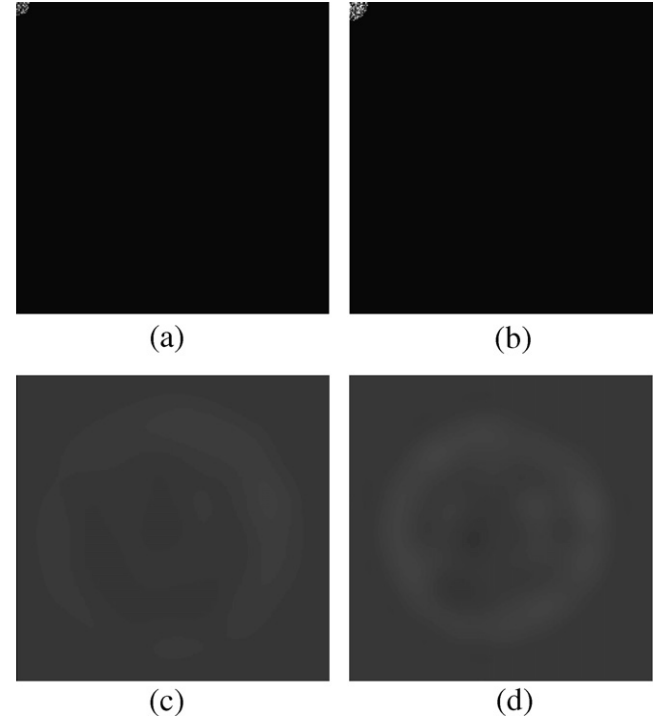

Fig. 3. (a and b) The respective DCT domain images of Fig. 2(a) and (b) with $D_{u,v} = 0$ (shown in blank) for all frequency components outside the sector of radius r^*; (c) and (d) the respective restored images.

tures are blurred and the edges of the SBL chips are apparently enhanced. The faultless surface results in an approximately uniform image, and the anomaly in the defective surface is notably enhanced in the restored image.

Fig. 5(a1)–(a4) are the restored images of the faultless surface in Fig. 2(a) when the sector radius is set at 5, 15, 35 or 65 pixels, and Fig. 5(b1)–(b4) are those of the defective surface in Fig. 2(b). For faultless surfaces, the larger the radius is used, the better the gray level uniformity is obtained in the restored images because more high-energy frequency components are removed. However, for defective surfaces, an overly large radius may severely blur the anomaly in the restored images, as seen in Fig. 5(b4). Therefore, the success of the global image reconstruction scheme for textured surface inspection lies in the selection of an appropriate radius that sufficiently removes random patterns and yet adequately reserves the anomalies in the restored images.

Let $E(r)$ denote the average energy of the sector with radius r,
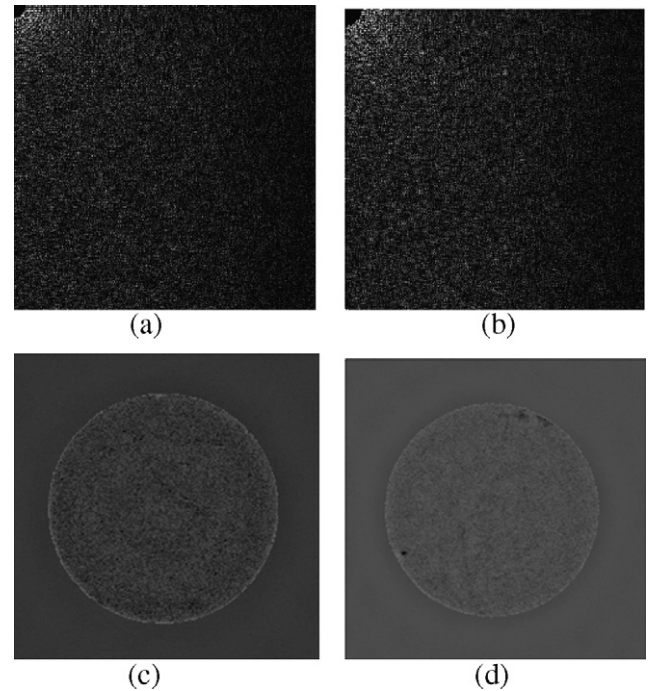

(a)

(b)

(c)

(d)

Fig. 4. (a and b) The respective DCT domain images of Fig. 2(a) and (b) with $D_{u,v} = 0$ for all frequency components inside the sector of radius r^*; (c) and (d) the respective restored images.

$$E(r) = \frac{1}{n_r} \sum_{u^2+v^2=r^2} P(u,v), \quad r = 1, 2, 3, \ldots, \sqrt{2}N$$
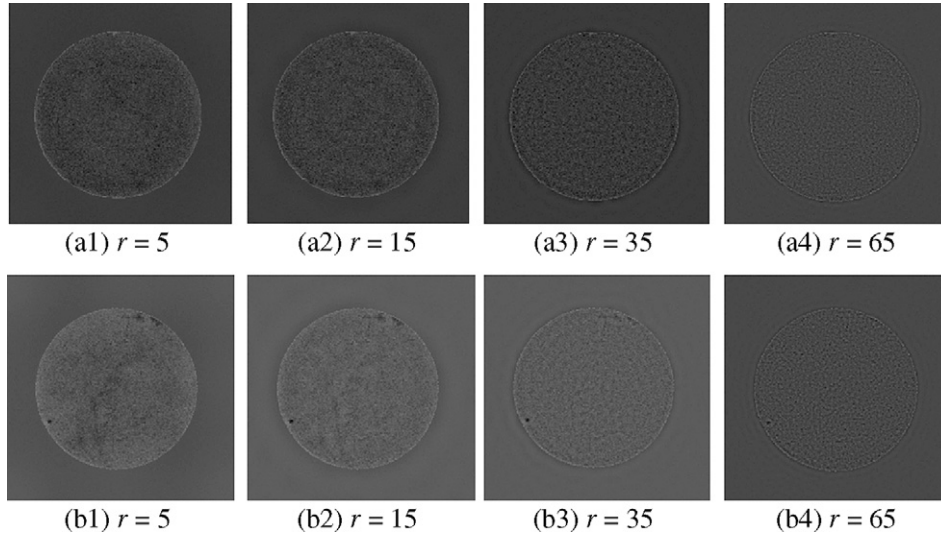
Fig. 5. (a1–a4) The restored images of the faultless SBL surface in Fig. 2(a); (b1)–(b4) the restored images of the defective SBL surface in Fig. 2(b) when the sector radius is set at 5, 15, 35 or 65 pixels.
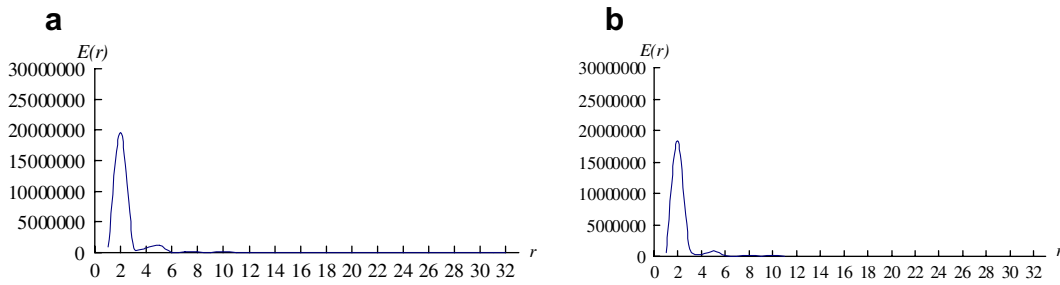

Fig. 6. (a and b) The plots of the average energy $E(r)$ as a function of radius r for the frequency matrices of SBL images in Fig. 2(a) and (b).

where n_r is the total number of points on the arc of radius r sector, and N is the image width. While the sector grows outwards from the top-left origin of the DCT spectrum, the average energy generally decreases rapidly. Fig. 6 plots the average energy $E(r)$ with respective to varying values of the radius r for Fig. 2(a) and (b). Note that the $E(r)$–r curves become flat soon after the radius r reaches the selected value in both the faultless and the defective images.

For exploring more regularities of the average energy plots, we decompose a frequency image array into four parts: odd–odd (o–o), odd–even (o–e), even–odd (e–o), and even–even (e–e) matrices based on the alternating decomposition of odd and even parts of the DCT frequency domain. Fig. 7 shows the average energy plots $E(r) - r$ of the four decomposed matrices in images with faultless and defective ones. It can be observed from Fig. 7(a1) and (b1) that high-energy frequency components are concentrated and distributed in the decomposed odd–odd matrix. We further plot the energy percentage diagrams of the decomposed matrices in the images with faultless and defective image shown in Fig. 8. They show that both of the decomposed odd–odd matrices (Fig. 7(a1) and (b1)), respectively, gather most (up to

90%) of the DCT energy in the two images. Thus, the odd–odd matrix can represent most information of the repetitive random texture of the SBL surface.

In most cases, the low frequency components (with larger magnitude) represent the global approximation of the original image. All other frequency components (middle and high frequency components) provide the local, detailed information of the image. Therefore, we can select a proper radius for the frequency components of larger magnitude to represent the global, repetitive textural feature of the image and remove such background texture by reconstructing the image without the use of larger-magnitude frequency components. In the following subsections, we propose a DCT decomposition and cumulative sum analysis procedure to automatically determine an appropriate sector radius for image reconstruction.

2.2. DCT decomposition

As given in Eq. (1), $D_{u,v}^{\#1}$ is the discrete cosine transform of a testing image $d_{x,y}^{\#1}$ of size $M \times N$. Let G^* be a waveform sign of 1-D frequency arrays and axis be a 1-D coordinate vector. Then, $G^*(\text{axis})$ is a waveform plot along the axis coordinate and can be denoted as:
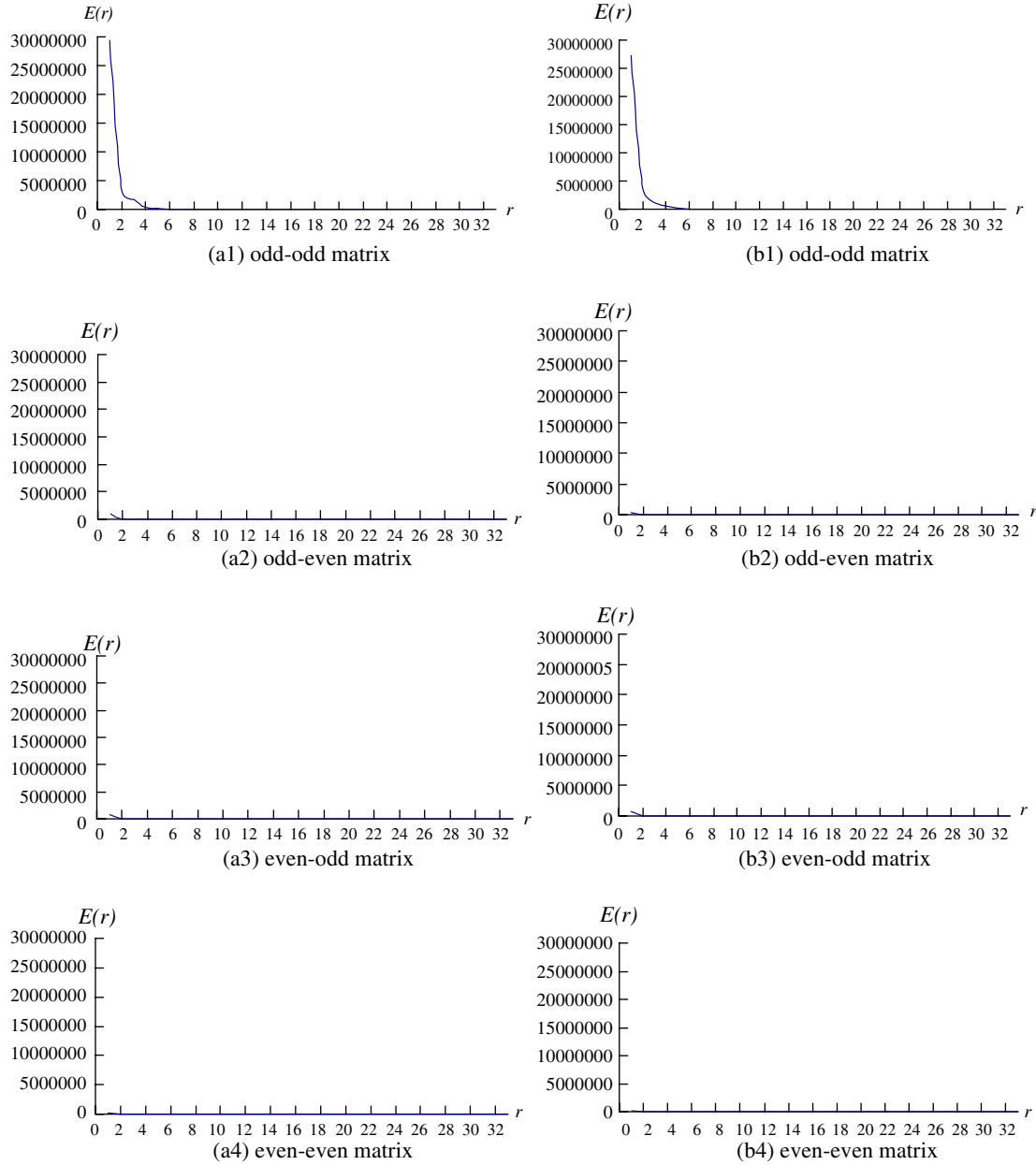
Fig. 7. (a1–a4) and (b1–b4) Average energy plots of the decomposed matrices for the SBL images in Fig. 2(a) and (b).

$$G^*(\text{axis}) = D^{\#1}_{u,v} \tag{4}$$

where axis $= D^{\#1}_{u,0\sim(N-1)}$ or $D^{\#1}_{0\sim(M-1),v}$; $u = 0, 1, 2,\ldots,M-1$; $v = 0, 1, 2,\ldots,N-1$. Fig. 9 shows the plots of 1-D waveform arrays $G^*(D^{\#1}_{0\sim(M-1),v})$ of a DCT frequency matrix along the u axis and demonstrates that the waveforms of the $G^*(D^{\#1}_{0\sim(M-1),v})$ remain stable until they approach the DC location. And, the closer the waveforms are to the DC location, the more widely they fluctuate. The magnitude of frequency components that are far away from the top left origin in the DCT domain falls rapidly and approximates zero.

We decompose the 2-D DCT domain $D^{\#1}_{u,v}$ into two matrices: the odd matrix $DO_{u,v'}$ and the even matrix $DE_{u,v'}$, whose definitions are given below:

$$DO_{u,v'} = D^{\#1}_{u,2v'} \tag{5}$$

$$DE_{u,v'} = D^{\#1}_{u,2v'+1} \tag{6}$$

where $u = 0, 1, 2,\ldots,M-1$; $v' = 0, 1, 2,\ldots,(N/2)-1$.

The odd-number frequencies of the v axis form the odd frequency matrix $DO_{u,v'}$, while the even-number frequencies make up the even frequency matrix $DE_{u,v'}$. The v' axis in either the odd or the even frequency matrix is half as long as the v axis in the original frequency matrix $D^{\#1}_{u,v}$.

Therefore, the original frequency matrix $D^{\#1}_{u,v}$ can be further decomposed into odd–odd $DOO_{u',v'}$, odd–even $DOE_{u',v'}$, even–odd $DEO_{u',v'}$, and even–even $DEE_{u',v'}$ matrices under the alternating decomposition of odd and even
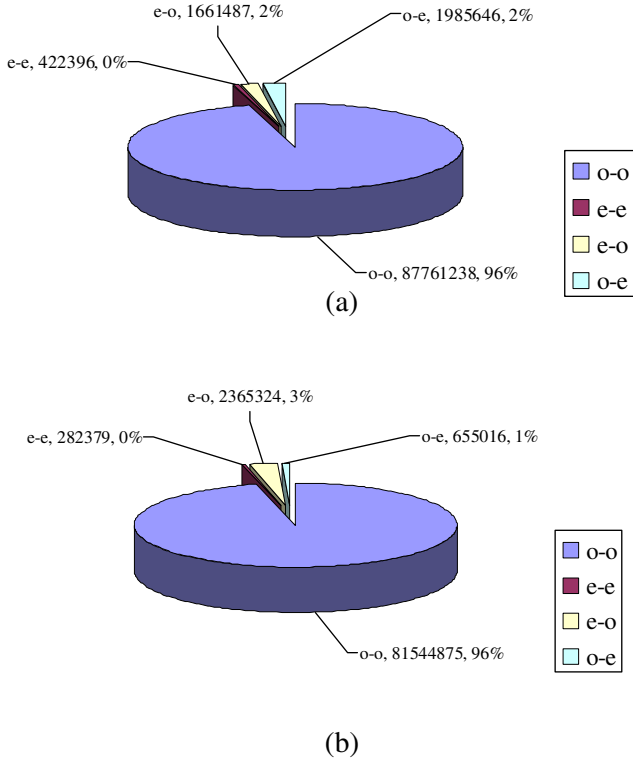
(a)

(b)

Fig. 8. (a and b) The energy percentage diagrams of the decomposed matrices for the SBL images in Fig. 2(a) and (b).

parts. These four matrices can be denoted as follows, respectively:

$$DOO_{u',v'} = D^{\#1}_{2u',2v'} \tag{7}$$

$$DOE_{u',v'} = D^{\#1}_{2u',2v'+1} \tag{8}$$

$$DEO_{u',v'} = D^{\#1}_{2u'+1,2v'} \tag{9}$$

$$DEE_{u',v'} = D^{\#1}_{2u'+1,2v'+1} \tag{10}$$

where $u' = 0, 1, 2, \ldots, (M/2) - 1$; $v' = 0, 1, 2, \ldots, (N/2) - 1$.

After the original frequency matrix $D^{\#1}_{u,v}$ is decomposed into four matrices (Eqs. (7)–(10)), we can use the G^* waveform plot to examine the frequency fluctuations of the waveform matrices. Since each frequency matrix has two dimensions, u' and v' axes, the four decomposed frequency matrices will have eight sets of 1-D waveform arrays.

Fig. 10 demonstrates the decomposition process of the u and v axes of a 2-D frequency matrix $D^{\#1}_{u,v}$.

To obtain the right sector radii that help improve the analysis results, the negative 45 degree diagonal coefficients of the frequency matrix can be decomposed into a 1-D array DA_t when M and N are equal and the top left DC location is set as the origin. This diagonal matrix can be denoted as follows:

$$DA_t = D^{\#1}_{t,t} \tag{11}$$

where $t = 0, 1, 2, \ldots, M - 1$.

The frequencies of the waveform plot $G^*(DA_t)$ of the matrix DA_t fluctuate in the same way as those of the waveform matrices $G^*(DO_{0\sim(M-1),v'})$ and $G^*(DE_{0\sim(M-1),v'})$. Thus, we can further decompose the matrix DA_t into $DAO_{t'}$ and $DAE_{t'}$ matrices. These two matrices can be denoted as follows:

$$DAO_{t'} = DA_{2t'} \tag{12}$$

$$DAE_{t'} = DA_{2t'+1} \tag{13}$$

where $t' = 0, 1, 2, \ldots, (M/2) - 1$. Fig. 11 shows the diagonal axis decomposition process of a 2-D DCT frequency matrix $D^{\#1}_{u,v}$.

After completing the decomposition procedure, we examine the frequency fluctuation trends of the waveform plots G^* of the four decomposed frequency matrices (Eqs. (7)–(10)). We find that the waveform plots of the 1-D odd arrays show significant and systematic frequency changes. The frequency fluctuation trends of the odd–odd matrix are smoother and more predictable when compared with those of the other decomposed matrices. The DCT frequency matrix $D^{\#1}_{u,v}$ needs to be decomposed because most of the regular waveform plots come from the decomposed odd–odd matrix $DOO_{u',v'}$. Therefore, the odd–odd frequency matrix $DOO_{u',v'}$ (including the diagonal matrix $DAO_{t'}$) will be the main target of the later analyses.

2.3. Cumulative sum algorithm for selecting the proper radius r^*

To select the proper sector radius, we propose a transition point detection method that use the DC location
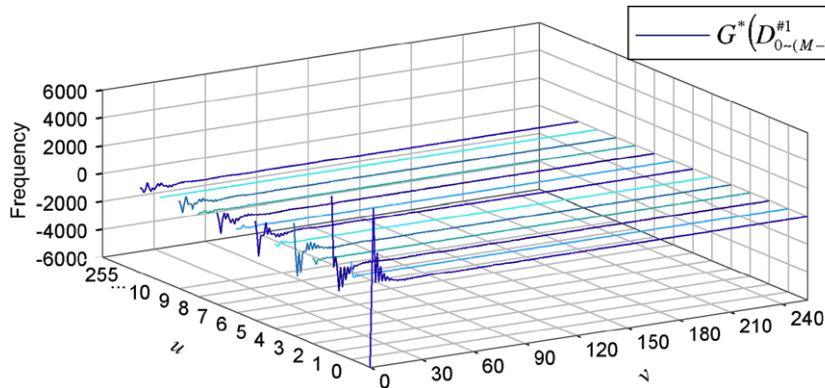

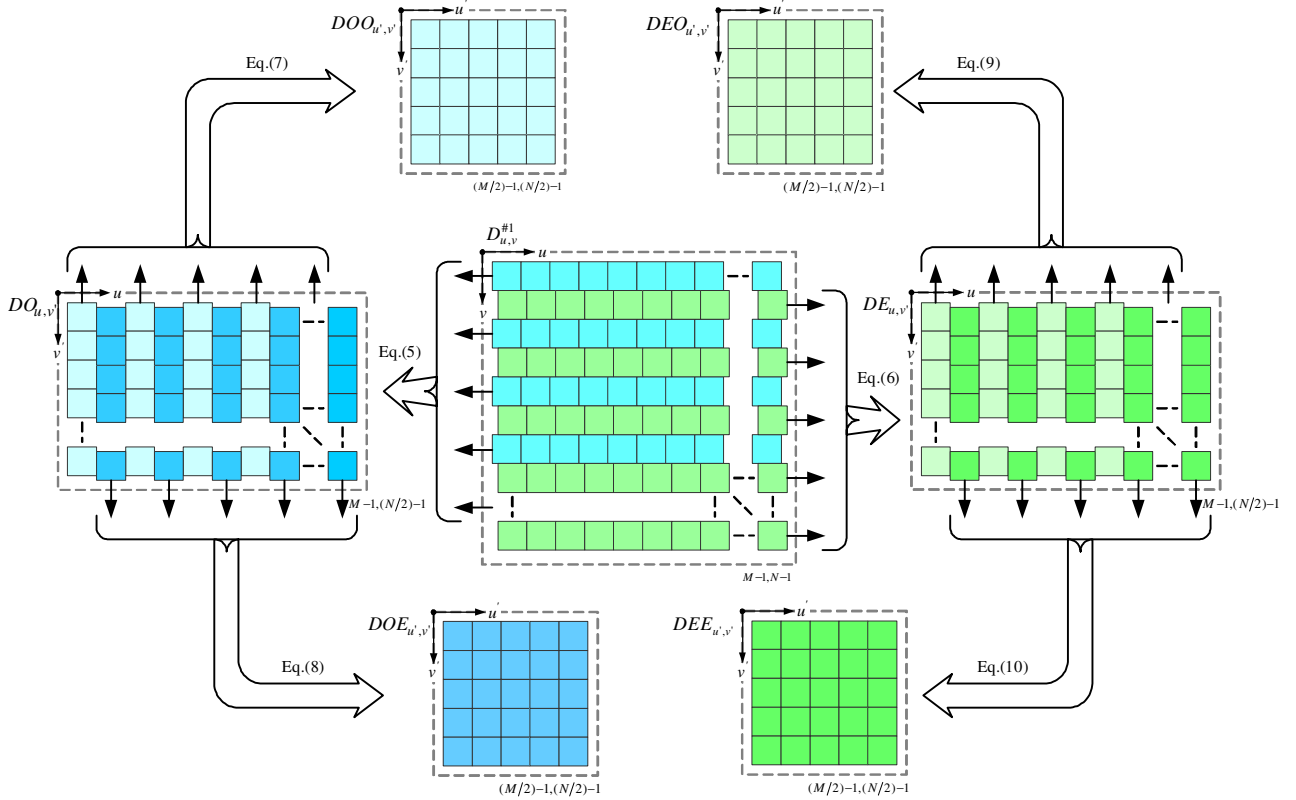Fig. 9. 1-D waveform plots $G^*(D^{\#1}_{0\sim(M-1),v})$.

Fig. 10. The decomposition process diagram of a 2-D DCT spectrum $D_{u,v}^{\#1}$ along the u and v axes.
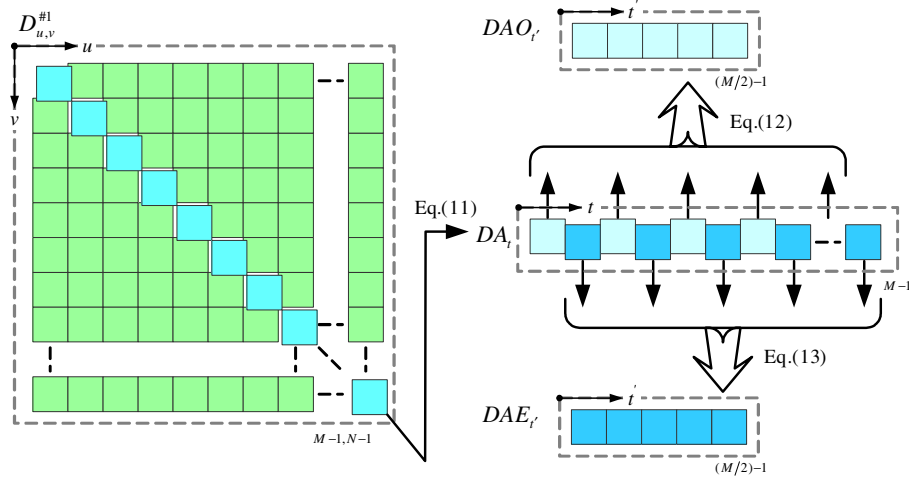

Fig. 11. The decomposition process diagram of a 2-D DCT spectrum $D_{u,v}^{\#1}$ along the diagonal axis.

as the origin of the sector area to locate the low-frequency regions. The proper radius r^* of the sector area is determined at the point where the frequency fluctuation trend gets stable. A stable frequency trend signifies that the frequencies are no longer in the low-frequency regions. Similar to the waveform plots G^*(axis) of the decomposed frequency matrices, the waveform plots of the decomposed odd–odd matrix $DOO_{u',v'}$ perform better

in detecting the transition point when the frequency trend turns stable. In addition, as the value increases along the axis, the amplitude of the waveform plots G^*(axis) decreases and so does their influence on the determination of the proper sector radius r^*. Therefore, this research analyzes three sets of frequency arrays $DOO_{u',0}$, $DOO_{0,v'}$, and $DAO_{t'}$ to determine the proper radius r^* of the sector.

The first value in each of the three frequency arrays $DOO_{u',0}$, $DOO_{0,v'}$ and $DAO_{t'}$ is the DC value in the DCT domain. This value represents the average gray level of an image in the spatial domain and is usually an extreme value (the largest or the smallest) in the frequency matrix. Hence, we set the DC value at zero when detecting the transition points in the gentle curves to determine the proper radius of the sector. Setting the DC value at zero can avoid significant variations among the frequency components. After the individual deviations of the three frequency arrays are calculated, three transition points can be identified in the gentle curves by the detection method. The proper radius of the sector r^* can be denoted as:

$$r^* = 2AVG(P_\alpha, P_\beta, P_\omega) + 1 \tag{14}$$

where $AVG(P_\alpha, P_\beta, P_\omega) = average(P_\alpha, P_\beta, \sqrt{2}P_\omega)$. The proper radius r^* is selected based on the average radius of the transition points of the gentle curves along the three principal frequency arrays in the decomposed odd–odd matrix. This proposed heuristic method determines the proper radius of the sector in the DCT domain for image reconstruction.

Fig. 12 shows that points P_α, P_β, and P_w are the three transition points of the gentle curves along u', v', and diagonal axes, respectively. The point P_w must be multiplied by a weight of $\sqrt{2}$ because this point comes from the diagonal matrix $DAO_{t'}$ and must be adjusted to be in the same scale as P_α and P_β. Fig. 13 depicts the three frequency arrays $DOO_{u',0}$, $DOO_{0,v'}$ and $DAO_{t'}$ of the odd–odd matrix $DOO_{u',v'}$ and their corresponding positions in the original DCT frequency matrix $D_{u,v}^{\#1}$. Since the u', v' and w' axes all come from the odd arrays of the original frequency matrix, the point obtained from the function AVG should be multiplied by 2 and then added by 1 to identify its original location in the DCT matrix.

2.3.1. Cumulative sum control scheme (CUSUM)

In Statistical Process Control (SPC), the cumulative sum (or cusum) control scheme performs well in detecting small process shifts. Cusum can effectively detect shifts of less than 1.5σ as well as indicate when the shifts probably occurred [32–34]. Hence, this research applies cusum to detect the transition points of gentle curves in frequency plots for computing the proper sector radius in the DCT domain. The cusum chart directly incorporates all the information in the sequence of sample values by plotting the cumulative sums of the deviations of the sample values from a target value. Suppose that Z sample sets with sample size $n = 1$ are collected, and X_z is the observation of the z-th sample, where $z = 1, 2, 3, \ldots, s, \ldots, Z$. Then, if μ_0 is the target value, the cumulative sum control chart is formed by plotting the quantity:

$$C_s = \sum_{z=1}^{s} (X_z - \mu_0) \tag{15}$$

where $s = 1, 2, 3, \ldots, Z$, and Eq. (15) can be further expressed as:

$$C_s = (X_s - \mu_0) + C_{s-1}. \tag{16}$$

The cusum scheme works by accumulating deviations from μ_0, which are above the target with one statistic C_s^+ and deviations from μ_0, which are below the target with one statistic C_s^-. The statistics C_s^+ and C_s^- are called one-sided upper and lower cusums, respectively. They are computed as follows [33]:

$$C_s^+ = \max[0, X_s - (\mu_0 + K) + C_{s-1}^+] \tag{17}$$
$$C_s^- = \max[0, (\mu_0 - K) - X_s + C_{s-1}^-] \tag{18}$$

where $C_0^+ = C_0^- = 0$, $K = \frac{\delta}{2}\sigma$.

In Eqs. (17) and (18), K as a reference value is often chosen about halfway between the target μ_0 and the out-of-control value of the mean μ_1 that we are interested in detecting quickly. Thus, if the shift is expressed in standard deviation units as $\mu_1 = \mu_0 + \delta\sigma$, then K is half the magnitude of the shift. When either C_s^+ or C_s^- exceeds the decision interval H, the sample set is considered to be out-of-control. The value for H is five times the standard deviation σ. This scheme distinguishes itself in that we can find the first period following the shift by counting backward from the out-of-control signal to the time period when the cusum lifted above zero.

2.3.2. Reverse order difference CUSUM method (RD-CUSUM)

CUSUM methods mainly process data that are smooth in the beginning periods and that deviate slightly in the later periods [33]. To suit the needs of this research, we reverse the order of the frequency array data because the curves of DCT frequency components fluctuate sharply in the beginning periods and then turn smooth in the other periods. We are able to apply the "reverse order" CUSUM method by moving backward those unstable data that are originally in the beginning periods and forward those smooth data that are originally in the later periods.

If the cumulative deviation sums reveal the trend of cyclic accumulations, then it means the data of the sequence
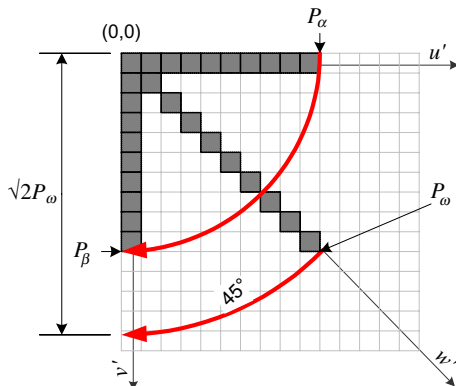

Fig. 12. A sector radius diagram obtained from transformation of the three principal frequency arrays.
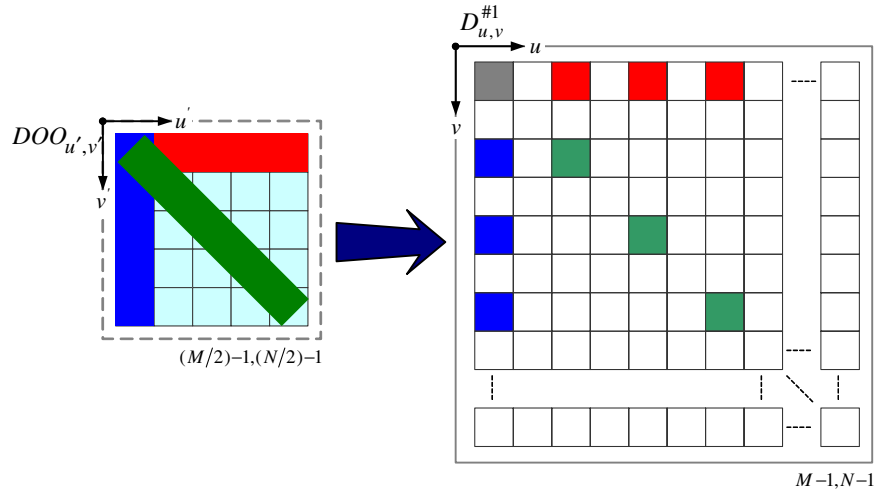
Fig. 13. The main elements of the odd–odd matrix $DOO_{u',v'}$ and their corresponding positions in the original DCT frequency matrix $D_{u,v}^{\#1}$.

are auto-correlated [33]. Cyclic accumulations may increase the chances of making wrong detection judgments and picking the wrong transition points. To overcome the problems of cyclic accumulations, we propose the reverse order difference CUSUM method (RD-CUSUM), which is also based on the CUSUM scheme to detect transition points. But, the RD-CUSUM method reverses the data sequence of the frequency array and calculates the difference between two successive data before the CUSUM algorithm is implemented. The difference function $L(x_z^*)$ calculates the new reverse-order difference sequence $L(x_{z-1}^*)$ by subtracting the reverse-order value x_{z-2}^* in period $(z-2)$ from the reverse-order value x_{z-1}^* in period $(z-1)$. Through the calculation of the reverse-order difference sequence, we can eliminate the cyclic accumulation phenomenon in the cumulative deviation sums.

We first arrange the data x_z^* of the frequency array in a reverse order and use $I(x_z^*)$ to denote the data in reverse permutation. Then, we calculate the difference between two successive data for all data and use $L(I(x_z^*))$ to denote the difference sequence $L(x_z^*)$ in reverse permutation. Finally, we can extend the CUSUM control scheme in Eqs. (17) and (18) to the case of the reverse-order difference sequence. We replace C_s^+ with C_z^+ (the one-sided upper cusum of the sequence $L(I(x_z^*))$), C_s^- with C_z^- (the one-sided lower cusum of the sequence $L(I(x_z^*))$), and X_s with $L(I(x_z^*))$, where μ_0 is the mean and σ the standard deviation of the sequence $L(I(x_z^*))$.

The data of the three arrays $DOO_{u',0}$, $DOO_{0,v'}$, and $DAO_{t'}$ are substituted into the sequence x_z^*, respectively. We proceed with the procedure of the RD-CUSUM method to identify the transition points $P(DOO_{u',0})$, $P(DOO_{0,v'})$, and $P(DAO_{t'})$ of the three frequency arrays and compute the best sector radius r^*. The calculation of the sector radius r^* by the RD-CUSUM method is shown in Fig. 14, from which we can see that the cyclic accumulations of the cumulative deviation sums are removed through the use of the difference function.

The RD-CUSUM method analyzes the frequency plots of the decomposed frequency arrays to locate transition points, which are points with abrupt changes of frequency values. The detection of transition points determines the proper sector radius for the frequency filtering operation, which greatly influences the later segmentation accuracy of the tiny defects.

2.4. Entropy method for defect segmentation

After the proper sector radius r^* is determined, the frequency filtering operation can accurately specify the non-defect low frequency regions and set the values of their frequencies at zero in the DCT domain. Then, we can transform the filtered frequency image back to the spatial domain for further defect separation. Thus, the filtered frequency image $D_{u,v}^{\#2}$ can be transformed back to the spatial domain to produce a corresponding restored image $d_{x,y}^{\#2}$ by using Eq. (2). When a restored image with enhanced tiny defects is generated, an automated thresholding technique called Kapur's entropy method is applied to separate the tiny defects from the normal regions.

Kapur's entropy method regards the image foreground and background as two different signal sources, so when the sum of the entropies of the two signal sources reaches its maximum, the image is said to be optimally thresholded [35]. Let us consider an image with gray levels in the range $[0, L-1]$. We assume S_l be the number of pixels in the image having gray level l and the total number of pixels in the image should be $\sum_{l=0}^{L-1} S_l$. Then, Y_l is an estimate of the probability of occurrence of gray level l in the image, denoted as $Y_l = S_l / \sum_{l=0}^{L-1} S_l$. From the definition of entropy, the entropy of an image is $N = -\sum_{l=0}^{L-1} Y_l \ln Y_l$. We aim to classify the pixels of the image into two opposite classes, namely defect (black) and normal region (white) by thresholding. The entropy of the defective portion of an image is $N_O(T)$ and the entropy of the normal portion of an image is $N_B(T)$. Therefore, Kapur's entropy method is
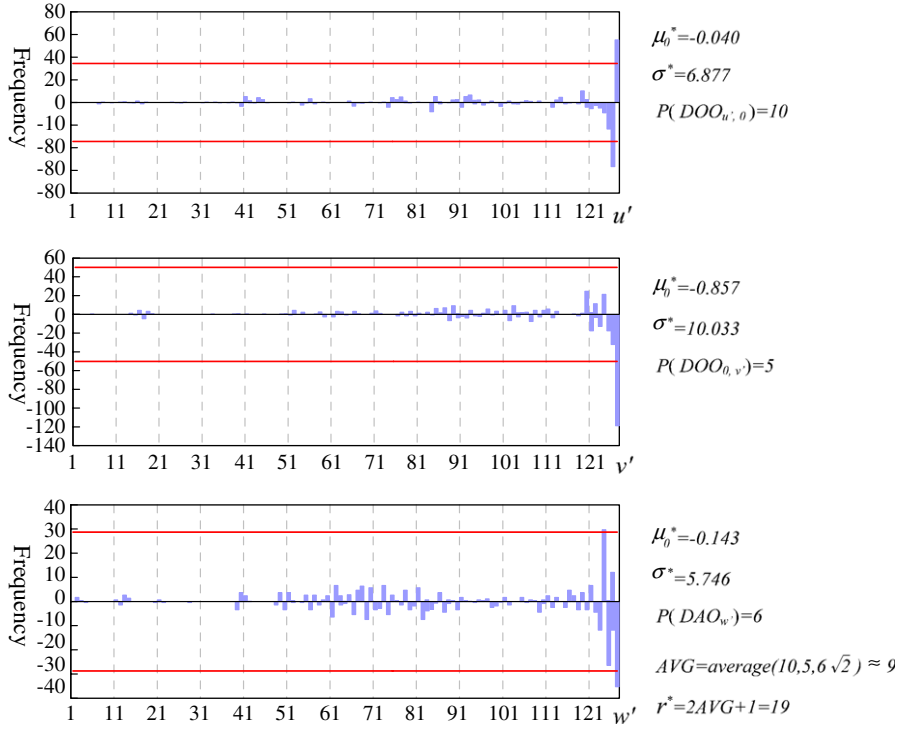
Fig. 14. An example of calculating the proper sector radius r^* by the RD-CUSUM method.

to determine the value of the threshold T, such that the total entropy N (Eq. (19)) of the partitioned image is maximized.

$$N = N_O(T) + N_B(T) = -\sum_{r=0}^{T} Y_r \ln Y_r - \sum_{r=T+1}^{L-1} Y_r \ln Y_r \quad (19)$$

Kapur's entropy method outperforms many other methods in detecting small objects [36]. However, the entropy method can not correctly separate tiny defects if the SBL image does not go through the defect enhancement step of the proposed DCT frequency filtering operation. This is because many noises in the image may incur erroneous judgment in defect separation. If an image is processed by the proposed DCT-based image reconstruction approach in advance, the tiny surface defects in the image can be precisely located by Kapur's entropy method.

3. Experiments and discussion

In this section, we implement the proposed approach and conduct experiments to evaluate its performance in detecting tiny surface defects. To strengthen the visibility of tiny surface defects, we make use of the following equipments: a white ring LED lighting device, a CCD (model WAT-221S of Watec company), a lens with changeable focal lengths and amplifications of 1–10 times, a frame grabber (model IMAQ PCI-1411 of National Instruments corporation), and an XYZ electronic control table with a controller. Each image of the SBL chip has a size of 256×256 pixels and a gray level of 8 bits. The

detection algorithm is edited in C language and executed on the sixth version of the C++ Builder complier on a personal computer (Pentium-4 2.66 GHz and 512 MB D-RAM).

3.1. Experimental results

3.1.1. Experiments with a small-sample size

To verify the feasibility of the proposed approach, 20 SBL chip images are first tested. Two (No. 12 and No. 20) of the 20 SBL chips contain no tiny defects, while each of the remaining 18 chips has at least one tiny defect. Table 1 summarizes the detection results of the 20 images. The features of detected defects include the number of detected defects, the number of their pixels, and the positions of their mass centers (X and Y coordinates). We evaluate the performances of the transition point detection method with respect to the following indices: statistics of detected results, numbers of erroneous judgments of defect detections, and area deviation rates of detected defects. The detection results in Table 1 indicates that the RD-CUSUM method identifies the transition points with great accuracy. The smaller the sector radius, the fewer frequency components are inside the selected sector and have their values set at zero in the DCT domain. A smaller than proper radius may result in identifying the normal regions as tiny defects or making the areas of the detected defects larger than those of the real defects. On the other hand, a larger than proper radius may result in identifying the tiny defects as normal regions or making the areas of the detected defects smaller than those of the real defects.

Table 1
Results of small-sample experiments

Samples	Image No.	1	2	3	4	5	6	7	8	9	10	11	12	13	14	15	16	17	18	19	20
	Real defect No.	1	1	1	1	1	1	1	1	1	1	1	0	1	1	1	1	1	1	1	0
	Pixels of a real defect	5	2	4	6	4	2	5	1	4	7	5		9	4	12	10	14	10	1	
RD-CUSUM	The selected radius r^*	11	15	13	15	13	9	17	15	15	9	15	9	11	11	13	13	9	11	13	9
	Detected defect No.	2	1	1	1	1	1	1	1	1	1	1	1	1	1	1	1	2	1	1	0
	Pixels of a detected defect	5, 1	2	4	6	4	2	5	1	4	7	5	1	9	4	12	10	14, 1	10	1	
	Mass center of a detected defect — X	169.2, 119	68	162.25	145	89.5	145	156.2	119.5	93.5	97	173.8	147	174.11	90.5	140.83	92.8	207, 90	105.5	180	
	Mass center of a detected defect — Y	145.4, 199	153	96.25	97.5	145.5	62.5	155.6	206.5	164.5	145	101.4	55	95.33	72.5	124	78.5	112.6, 195	74.6	185	

As Table 1 indicates, the RD-CUSUM method can accurately identify the locations and the areas (pixels) of tiny defects. The mass centers of the defects detected by the RD-CUSUM method are all very close to the real ones. Besides, the areas of most defects in the 20 images are accurately measured; only in images Nos. 1, 12, and 17 are the normal regions mistakenly identified as 1-pixel defects. Since tiny defects are extremely small, how accurately a method measures the area of a detected defect becomes extraordinarily important in comparing the detection performance of various methods. Moreover, the RD-CUSUM method is competent in detecting tiny defects of varying sizes and computing their areas. For instance, the actual defect area in image No. 17 is as large as 14 pixels and the actual defect areas of images No. 8 and No. 19 are as small as 1 pixel each. A simplified version of Table 1 is given in Table 2 to facilitate further discussion of the detection results.

In Table 2, the RD-CUSUM method is evaluated by the three indices: Type I error α (false alarms, which regard normal regions as defects.), Type II error β (missing alarms, which fail to alarm real defects), and area deviation rates of detected defects. We divide the number of erroneously detected defects by the number of total testing images to obtain Type I error α, and the number of missing defects by the number of total defects to obtain Type II error β. To compute the area deviation rate of detected defects, we first add up the differences between the correctly detected defect areas and their corresponding actual defect areas; and then divide the summation by the total actual defect areas. For all of the three indices, the smaller the index value, the better the detection result.

As Table 2 indicates, the RD-CUSUM method achieves great performance in detecting the number of correctly detected defects. Type I error of the RD-CUSUM method is 0.15; and its Type II errors is 0%. When the major concern of detection is on the accurate areas of the detected defects, the RD-CUSUM method should be applied because of its accuracy in detecting defect areas. The area deviation rate of a detected defect signifies how inaccurately the method detects the area of a defect. The area deviation rate of the method is 3.8%. The results of our small-sample experiments show that the proposed method has great feasibility and good performances. To verify the results, experiments with large testing samples are conducted in the following subsection.

3.1.2. Experiments with a large-sample size

To conduct a large-sample experiment, another 120 SBL chip images are tested. Each of the first 100 of the 120 SBL chips contains at least one tiny defect, while the remaining 20 are regular chips without any tiny defect. The proposed approach takes an average of 4 s to process a forward and an inverse DCT transformations. The processing time can be significantly shortened if the DCT functionality is incorporated into a single integrated circuit. Actually, if we do not count the time of the forward and inverse DCT steps,

Table 2
Simplified results of small-sample experiments

Method	Number of real defects	Number of correctly detected defects	Number of erroneously detected defects	Number of missing defects	Type I error (α)	Type II error (β) (%)	Area deviation rate of detected defects (%)
RD-CUSUM	18	18	3	0	0.15	0.00	3.80

it takes less than 10 ms for the RD-CUSUM method to process an SBL chip. This means that the methods used in this research are very time-saving and efficient.

Table 3 presents the results of large-sample experiments in which we demonstrate the performance of the proposed method based on the number of total real defects. Table 3 shows the experimental results of detecting the 120 testing images which contain a total of 114 real tiny defects. The statistics are computed based on the number of total real defects, and the results are consistent with those of the previous preliminary experiment. The RD-CUSUM method has low Type I error value (0.1) and Type II error value (5.26%). In addition, this method also has a small area deviation rate (4.81%), which implies that the areas of the detected defects are the closest to those of real defects.

3.2. Experiments on DCT reconstruction effects

To evaluate the performance of the proposed DCT-based image reconstruction approach, experiments with and without the defect enhancement process are both conducted. The testing images with and without the DCT defect enhancement operation are all segmented by Kapur's entropy method to examine how they differ in terms of tiny defect detection. The testing samples as well as the experimental configurations and procedures are the same as those of the large-sample experiments. Based on the number of total real defects, Table 4 presents the performance evaluation indices of tiny defect detection with and without the DCT defect enhancement process.

Table 4 shows that the method with DCT defect enhancement has significantly lower Type I error and area

Table 3
Results of large-sample experiments

Method	Number of total real defects	Number of correctly detected defects	Number of erroneously detected defects	Number of missing defects	Type I error (α)	Type II error (β) (%)	Area deviation rate of detected defects (%)
RD-CUSUM	114	108	18	6	0.15	5.26	4.81

Table 4
The performance evaluation table of defect detection with and without DCT defect enhancement process

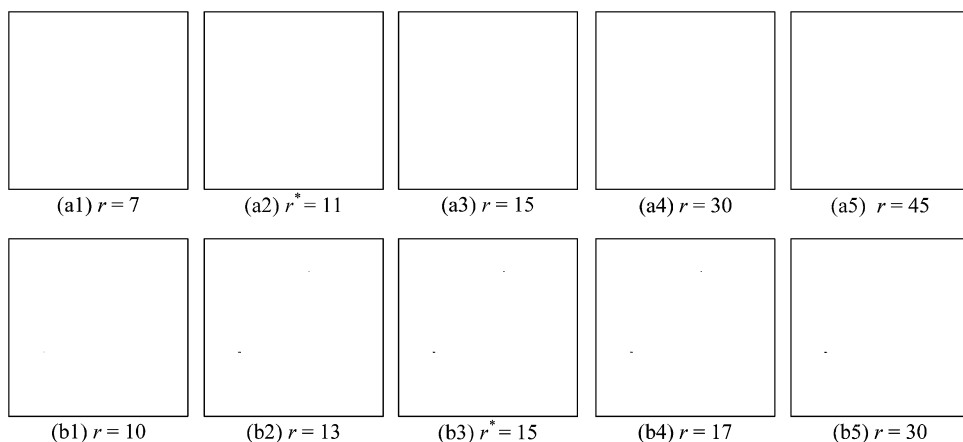| Method	Number of total real defects	Number of correctly detected defects	Number of erroneously detected defects	Number of missing defects	Type I error (α)	Type II error (β) (%)	Area deviation rate of detected defects (%)
DCT defect enhancement + entropy	114	108	18	6	0.158	5.26	4.81
Entropy	114	103	64	11	0.561	9.65	212.50

Fig. 15. (a1–a5) The resulting binary images from the sectors of radii 7, 11, 15, 30 and 45 pixels for the faultless SBL surface in Fig. 2(a); (b1)–b(5) the resulting binary images from the sectors of radii 10, 13, 15, 17, and 30 pixels for the defective SBL surface in Fig. 2(b).

deviation rate than the method without DCT defect enhancement. The proposed method outperforms the method without DCT defect enhancement in reducing the Type I error by 72% and the area deviation rate by 98%. The comparison results of the experiments clearly and objectively demonstrate the great performance of the proposed DCT-based image reconstruction approach in detecting tiny defects.

3.3. Sensitivity analysis of the proposed method

3.3.1. Sensitivity of the selected radius r^*

In this study, the proper radius r^* used for image reconstruction is selected based on the abrupt changes of the fre-quency coefficients in the decomposed odd–odd matrix. A faultless SBL surface and a defective one, as shown in Fig. 2(a) and 2(b), are used to evaluate the sensitivity of minor changes in r^* value. Fig. 15(a1)–(a5) present the final results from sector radii of 7, 11, 15, 30 and 45 pixels for the faultless texture in Fig. 2(a), in which $r^* = 11$ given significantly abrupt change of frequency values. Fig. 15(b1)–(b5) present the final results from radii of 10, 13, 15, 17 and 30 pixels for the defective texture in Fig. 2(b), in which $r^* = 15$. From Fig. 15 we find that the radii in the neighborhood of the selected r^* generates similar final results. It is not crucial for the selection of a precise r^* value. The image reconstruction process can tolerate minor changes of the selected radius r^*. Experiments results show that a minor
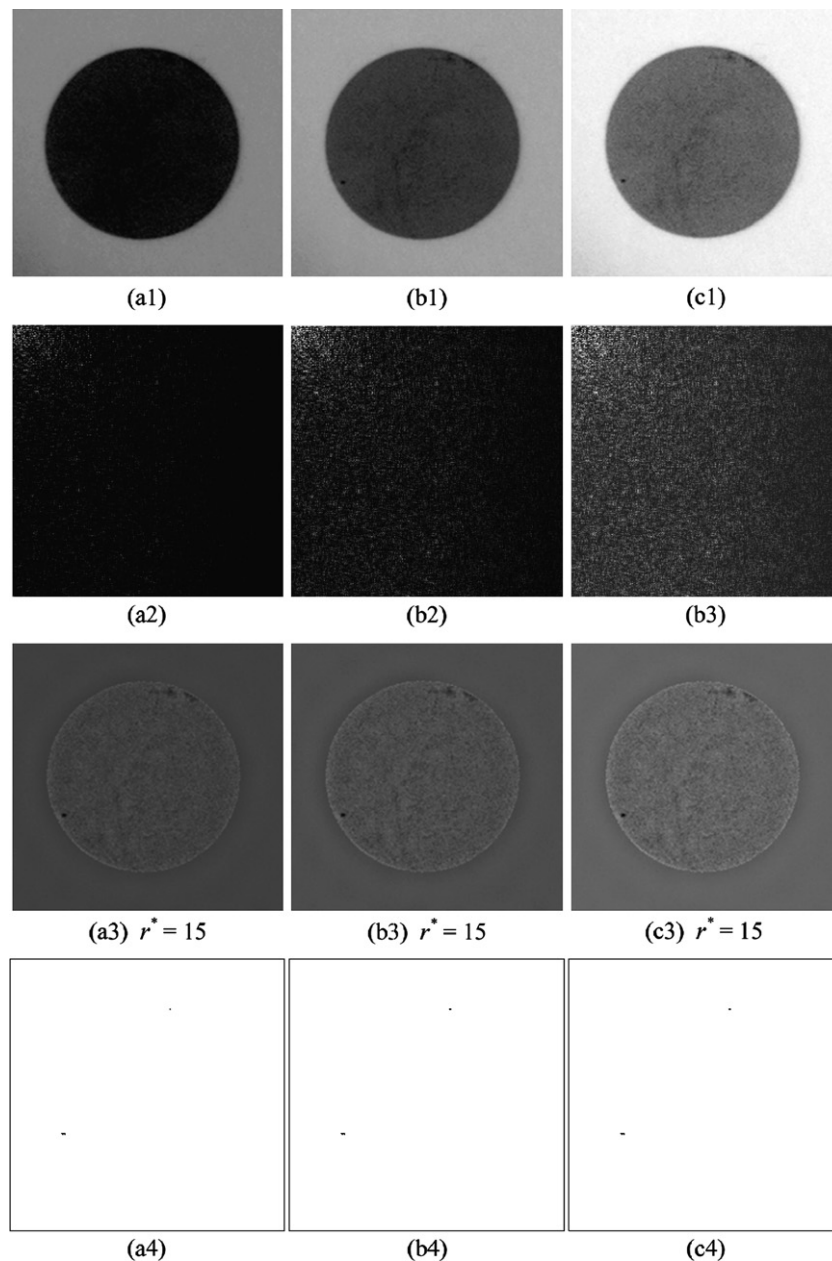

Fig. 16. The effect of changes in illumination intensity: (a1)–(c1) a defective SBL surface under regular, underexposed and overexposed lighting conditions; (a2)–(c2) the respective DCT domain images; (a3)–(c3) the respective restored images; (a4)–(c4) the resulting binary images that show the defects in black.
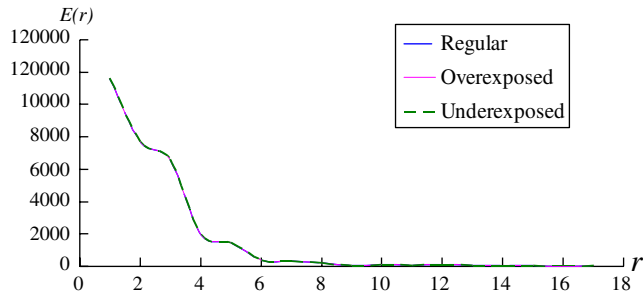
Fig. 17. The plots of $E(r)$–r curves of the odd–odd matrices for the SBL images in Fig. 16(a1)–(c1).

change of r^* values between 1 and 4 pixels will not affect the reconstruction result.

3.3.2. Changes of illumination intensity

The proposed method in this research is based on a global image reconstruction scheme for defect detection. It is insensitive to changes in the illumination intensity. Fig. 16(b1) shows a defective SBL surface under regular lighting condition. Fig. 16(a1) and (c1) are underexposed and overexposed versions of the SBL image in Fig. 16(a1). Fig. 17 depicts the $E(r)$–r curves of the odd–odd matrices for the SBL images in three different illumination intensities. The selected radii r^* for Fig. 16(a1)–(a3) are the same as 15 pixels. Fig. 16(a2)–(c2) and (a3)–(c3), respectively, presents the DCT domain images and the restored images of the three SBL images. Fig. 16(a4)–(c4) shows the defect detection results of Fig. 16(a3)–(c3) as
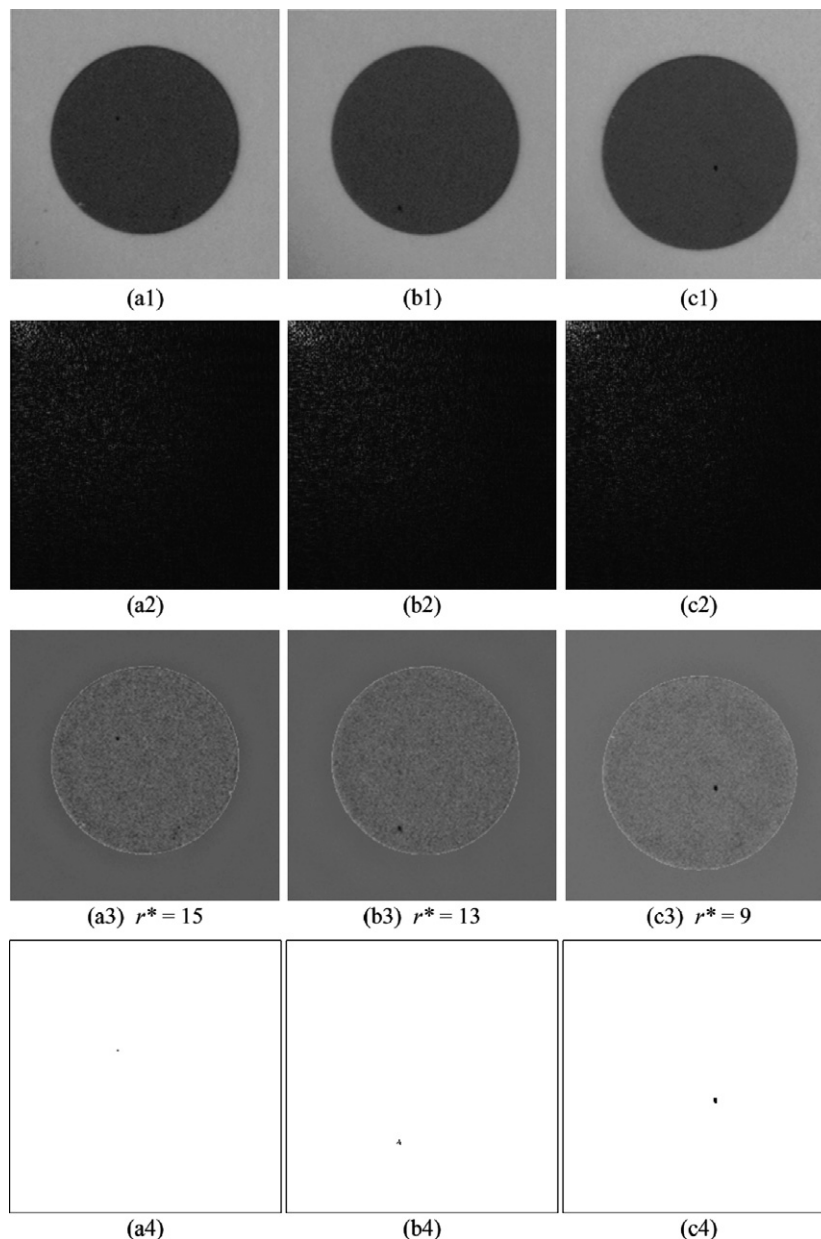

Fig. 18. The effect of changes in size for defects in SBL: (a1)–(c1) SBL images containing increasing sizes (2, 8, 14 pixels) of defects; (a2)–(c2) the respective DCT domain images; (a3)–(c3) the respective restored images; (a4)–(c4) the resulting binary images that show the defects in black.

resulting binary images. The results reveal that the defects in all three SBL images are correctly separated in the binary images, regardless of lighting changes.

3.3.3. Various sizes and numbers of defects in an image

To explore how the proposed method detects defects of different sizes, Fig. 18(a1)–(c1) presents defects in increasing sizes (2, 8 and 14 pixels) on SBL surfaces. The detection results in Fig. 18(a3)–(c3) indicate that the defects are well enhanced in the restored images, even though the actual defect area is as small as 2 pixels or as large as 14 pixels. Nevertheless, defects of large sizes cannot be completely detected because the central parts of the defects may be removed after the high-pass filtering procedure is conducted.

To examine how the proposed method detects various numbers of defects in an image, Fig. 19(a1)–(c3) presents increasing numbers (4, 5 and 7) of defects on SBL surfaces. The resulting binary images in Fig. 19(a4)–(c4) demonstrate that tiny defects are well detected, even though a large number of tiny defects exist in the same image. Experiments results show that the performance of the proposed method is not restricted by the number of defects in an image.
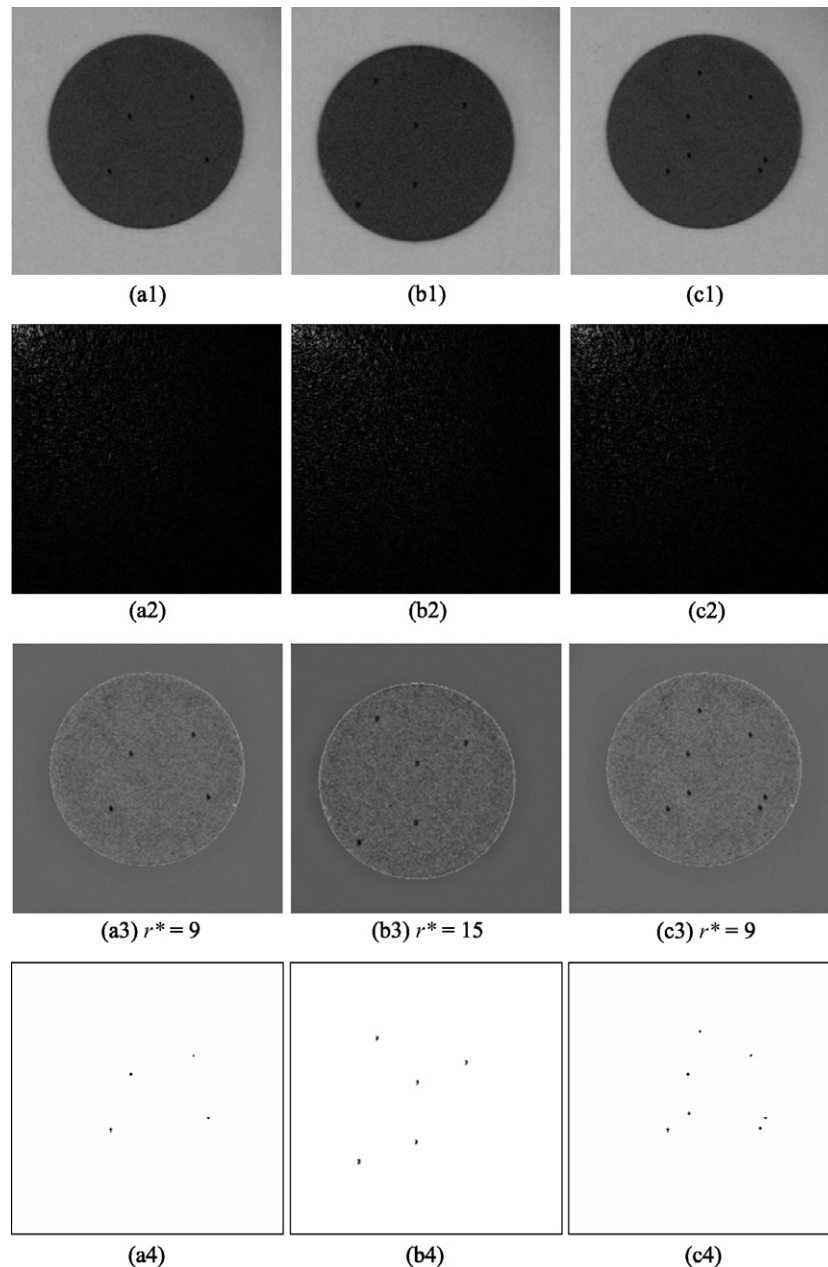

Fig. 19. The effect of changes in defect number in an image: (a1)–(c1) SBL images containing increasing numbers (4, 5, 7) of defects; (a2)–(c2) the respective DCT domain images; (a3)–(c3) the respective restored images; (a4)–(c4) the resulting binary images that show the defects in black.

4. Conclusion

This paper presents a global approach for the automated visual inspection of tiny defects in the surfaces of SBL chips. Unlike conventional feature extraction methods, the proposed method relies on no textural features. Based on an image reconstruction scheme, it applies DCT decomposition and cumulative sum techniques to effectively detect tiny defects. DCT has the advantages of packing the most information into the fewest coefficients and minimizing reconstruction errors. By analyzing the energy concentration condition of a SBL frequency image, we can apply the DCT-based approach to decompose the frequency domain image into four decomposed matrices. From the decomposed odd–odd matrix, the cumulative sum algorithm can be used to select proper frequency values of large magnitude that represent the normal background texture of the SBL surface. Then, we take out the selected frequency values of large magnitude and reconstruct the image from the DCT frequency matrix to remove the global random patterns of the statistically textured image and reserve local anomalies in the reconstructed image.

The proposed method is based on a global image reconstruction scheme for defect detection and is insensitive to changes in illumination intensity. If lighting changes lead to underexposed or overexposed lighting conditions, only the values of the DC components will be changed after the DCT transformation. Changes of the DC values do not affect the detection results of the proposed method. Performance of the proposed method can be limited by defect size, background property, and processing time. Defects of large sizes cannot be completely detected because the central parts of the defects may be removed after the high-pass filtering procedure is conducted. Defects embedded in structural textures cannot be detected because the proposed method is suitably applied to identify defects in random textures. The proposed method takes 4 s to process a forward and an inverse DCT transformations in our experimental configurations. This processing time can be significantly decreased to meet the requests of on-line automatic inspection by implementing the proposed approach in a single integrated circuit.

The proposed method is effective and efficient in detecting tiny defects of different kinds, which include dust, cavities and pinholes on the surfaces of SBL chips. Experimental results show that the proposed method outperforms the traditional approach in reducing the Type I error by 72% and in decreasing the deviation of the defect areas by 98%. Future research can make use of the research results and investigate the following areas: a global DCT-based enhancement approach for detecting tiny surface defects in structural textures, and the proposed DCT decomposition procedure applied in the image compression and feature extraction fields.

References

[1] D.M. Stubbs, S.H. Pulko, A.J. Wilkinson, B. Wilson, F. Christiaens, K. Allaert, Embedded passive components and PCB size-thermal effects, Microelectronics International 17 (2) (2000) 7–10.

[2] R.R. Tummala, G.E. White, V. Sundaram, S.K. Bhattacharya, SOP: the microelectronics for the 21st century with integral passive integration, Advancing Microelectronics 27 (1) (2000) 13–19.

[3] Chi-Hao Yeh, Ta-Cheng Shen, Ful-Chiang Wu, A case study: passive component inspection using a 1D wavelet transform, International Journal of Advanced Manufacturing Technology 22 (2003) 899–910.

[4] D.M. Tsai, C.Y. Hsieh, Automated surface inspection for directional textures, Image and Vision Computing 18 (1999) 49–62.

[5] Du-Ming Tsai, Tse-Yun Huang, Automated surface inspection for statistical textures, Image and Vision Computing 21 (2003) 307–323.

[6] C.J. Lu, D.M. Tsai, Defect inspection of pattern thin film transistor-liquid crystal display panels using a fast sub-image-based singular value decomposition, International Journal of Production Research 42 (20) (2004) 4331–4351.

[7] Chi-Jie Lu, Du-Ming Tsai, Automatic defect inspection for LCDs using singular value decomposition, International Journal of Advanced Manufacturing Technology 25 (2005) 53–61.

[8] B.C. Jiang, C.C. Wang, H.C. Liu, Liquid crystal display surface uniformity defect inspection using analysis of variance and exponentially weighted moving average techniques, International Journal of Production Research 43 (1) (2005) 67–80.

[9] Wen-Yen Wu, Mao-Jiun J. Wang, Chih-Ming Liu, Automated inspection of printed circuit boards through machine vision, Computers in Industry 28 (1996) 103–111.

[10] C.H. Yeh, D.M. Tsai, A rotation-invariant and non-referential approach for ball grid array (BGA) substrate conducting path inspection, International Journal of Advanced Manufacturing Technology 17 (2001) 412–424.

[11] Du-Ming Tsai, Cheng-Huei Chiang, Automatic band selection for wavelet reconstruction in the application of defect detection, Image and Vision Computing 21 (2003) 413–431.

[12] A. Pikaz, A. Averbuch, An efficient topological characterization of gray-levels textures using a multiresolution representation, Graphical Models and Image Processing 59 (1997) 1–17.

[13] L.H. Siew, R.M. Hodgson, L.K. Wee, Texture measures for carpet wear assessment, IEEE Transactions on Pattern Analysis and Machine Intelligence 10 (1988) 92–150.

[14] A.L. Amet, A. Ertuzun, A. Ercil, An efficient method for texture defect detection: sub-band domain co-occurrence matrices, Computers and Geosciences 28 (2002) 763–774.

[15] M. Tico, P. Kuosmanen, J. Saarinen, Wavelet domain features for fingerprint recognition, Electronics Letters 37 (1) (2001) 21–22.

[16] Hamed Sari-Sarraf, J.S. Goddard, Robust defect segmentation in woven fabrics, Proceedings of Computer Vision and Pattern Recognition (1998) 938–944.

[17] H. Rau, C.H. Wu, Automatic optical inspection for detecting defects on printed circuit board inner layers, International Journal of Advanced Manufacturing Technology 25 (2005) 940–946.

[18] Chi-Hao Yeh, Fang-Chih Tien, Ful-Chiang Wu, Boundary-based passive component inspection approach using eigenvalues of covariance matrices, International Journal of Production Research 41 (17) (2003) 4025–4040.

[19] N. Ahmed, T. Natarajan, K.R. Rao, Discrete cosine transform, IEEE Transactions on Computer 23 (1) (1974) 90–93.

[20] Yui-Lam Chan, Wan-Chi Siu, Variable temporal-length 3-D discrete cosine transform coding, IEEE Transactions on Image Processing 6-5 (1997) 758–763.

[21] Mandyam Giridhar, Nasir Ahmed, Neeraj Magotra, Lossless image compression using the discrete cosine transform, Journal of Visual Communication and Image Representation 8 (1) (1997) 21–26.

[22] Zhishun Wan, Zhenya He, Cairong Zou, J.D.Z. Chen, A generalized fast algorithm for n-D discrete cosine transform and its application to motion picture coding, IEEE Transactions on Circuits and Systems-II: Analog and Digital Signal Processing 46 (5) (1999) 617–627.

[23] K.R. Rao, J.J. Hwang, Techniques and Standards for Image, Video, and Audio Coding, Prentice-Hall, Inc., 1996.

[24] Ming-Ting Sun, I-Ming Pao, Statistical computation of discrete cosine transform in video encoders, Journal of Visual Communication and Image Representation 9–2 (1998) 163–170.

[25] Nam Ik Cho, Sang Uk Lee, Fast algorithm and implementation of 2-D discrete cosine transform, IEEE Transactions on Circuits and Systems 38 (3) (1991) 297–305.

[26] C.W. Kok, Fast algorithm for computing discrete cosine transform, IEEE Transactions on Signal Processing 45 (3) (1997) 757–760.

[27] Yuh-Ming Huang, Ja-Ling Wu, A refined fast 2-D discrete cosine transform algorithm, IEEE Transactions on Signal Processing 47 (3) (1999) 904–907.

[28] Biao Chen, Shahram Latifi, Junichi Kanai, Edge enhancement of remote sensing image data in the DCT domain, Image and Vision Computing 17 (12) (1999) 913–921.

[29] Md. Kamrul Hasan, Sayeef Salahuddin, M. Rezwan Khan, Reducing signal-bias from MAD estimated noise level for DCT speech enhancement, Signal Processing 84 (2004) 151–162.

[30] Tae Yong Kim, Joon Hee Han, Model-based discontinuity evaluation in the DCT domain, Signal Processing 81 (2001) 871–882.

[31] Rafael C. Gonzalez, Richard E. Woods, Digital Image Processing, 2nd ed., Prentice Hall, 2002.

[32] F.F. Gan, An optimal design of CUSUM quality control charts, Journal of Quality Technology 23 (4) (1991) 279–286.

[33] Douglas C. Montgomery, Introduction to Statistical Quality Control, 5th ed., John Wiley & Sons, 2005.

[34] J.J. Pignatiello Jr., G.C. Runger, Comparison of multivariate CUSUM charts, Journal of Quality Technology 22 (3) (1990) 173–186.

[35] J. Kapur, P. Sahoo, A. Wang, A new method for gray-level picture thresholding using the entropy of the histogram, Computer Vision, Graphics, and Image Processing 29 (1985) 273–285.

[36] M. Sezgin, B. Sankur, Survey over image thresholding techniques and quantitative performance evaluation, Journal of Electronic Imaging 13 (1) (2004) 146–165.